Tectonics

RESEARCH ARTICLE
10.1029/2020TC006389

Key Points:

- Regional average strain rate across the Great Basin from 15-ka fault slip rates shows a strain concentration in the Walker Lane (WL)
- Geologic and geodetic velocity fields show similar patterns but different magnitudes in the WL, suggesting missing shear in the geologic record
- Tectonic history, fault slip rates, and GPS data are consistent with the Sierra Nevada as a rigid boundary of the continuously deforming WL

Supporting Information:

- Supporting Information S1
- Supporting Information S2
- Table S1
- Table S2

Correspondence to:
N. G. Reitman,
nreitman@usgs.gov

Citation:
Reitman, N. G., & Molnar, P. (2021). Strain and velocity across the Great Basin derived from 15-ka fault slip rates: Implications for continuous deformation and seismic hazard in the Walker Lane, California-Nevada, USA. *Tectonics*, *40*, e2020TC006389. https://doi.org/10.1029/2020TC006389

Received 17 JUN 2020
Accepted 30 JAN 2021

Strain and Velocity Across the Great Basin Derived From 15-ka Fault Slip Rates: Implications for Continuous Deformation and Seismic Hazard in the Walker Lane, California-Nevada, USA

Nadine G. Reitman[1,2] **and Peter Molnar**[1,3]

[1]Department of Geological Sciences, University of Colorado Boulder, Boulder, CO, USA, [2]Now at U.S. Geological Survey, Golden, CO, USA, [3]Cooperative Institute for Research in Environmental Science (CIRES), University of Colorado Boulder, Boulder, CO, USA

Abstract Average strain across the Great Basin over the past 15 Kyr derived from slip rates on individual faults shows a concentration of both right-lateral shear and extension in the western Great Basin (Walker Lane). Straining is modest across the central Great Basin, with a zone of higher strain in the eastern Great Basin including the Wasatch Front. The horizontal velocity field derived from 15-ka fault slip rates is similar to the pattern of GPS velocities, suggesting that regional strain release patterns have been constant over the past 15 Kyr. The magnitudes of velocities inferred from fault slip rates, relative to North America, are lower than those from GPS in the Walker Lane, suggesting that the geologic record is missing evidence of strike slip on faults, and seismic hazard may be higher than suggested by fault slip rates alone. The observed strain concentration in the western Great Basin is consistent with a Sierra Nevada block that is more rigid than the surrounding lithosphere of nonlinear rheology, which concentrates strain east of and adjacent to the rigid block. Treating the western U.S. as a thin viscous sheet with the Sierra Nevada block as a rigid boundary provides a consistent history of continuous deformation in the Walker Lane over decadal, millennial, and Neogene timescales.

Plain Language Summary Slip rates on some active faults determined from decadal GPS measurements disagree with geologic estimates based on offset accrued over 1,000s of years. We use two databases of fault slip rates to calculate deformation rates across the Basin and Range province of the western U.S. over the past 15,000 years and compare results to deformation rates from decadal GPS data and 13-million-year reconstructions of tectonic plate movements on a regional scale. Decadal and 15,000-year deformation rates are similar in pattern but differ in magnitude in the area of the western U.S. that lies within ~150 km of the eastern edge of the Sierra Nevada, called the Walker Lane. The results suggest that the Walker Lane is an approximately 150-km-wide zone of concentrated strain, and evidence of slip on faults in the Walker Lane is missing from the databases used to calculate probabilistic seismic hazard. The pattern of deformation suggests that the Earth's brittle crust is broken into small blocks whose relative movement is dictated by continuous deformation of the ductile uppermost mantle, which behaves as a viscous fluid.

1. Introduction

Whether intracontinental deformation is best described by motion of effectively rigid blocks sliding past one another on discrete faults or as a continuum is a widely discussed question in tectonics. These two views are not entirely in opposition because the relative movements of a large number of small blocks resembles a deforming continuum. The underlying debate, therefore, rests on the role of faults in the shallow, brittle crust. Knowledge of the length of a fault helps determine the maximum magnitude of an earthquake on the fault, and the slip rate on a fault helps determine the average recurrence interval of such an earthquake. Therefore, a description of the deformation field in terms of faults and blocks is useful for earthquake hazard assessment, but offers little help in understanding the dynamic processes that govern large-scale deformation. Treating intracontinental deformation as a continuum enables the kinematics of deformation to be understood in terms of dynamics.

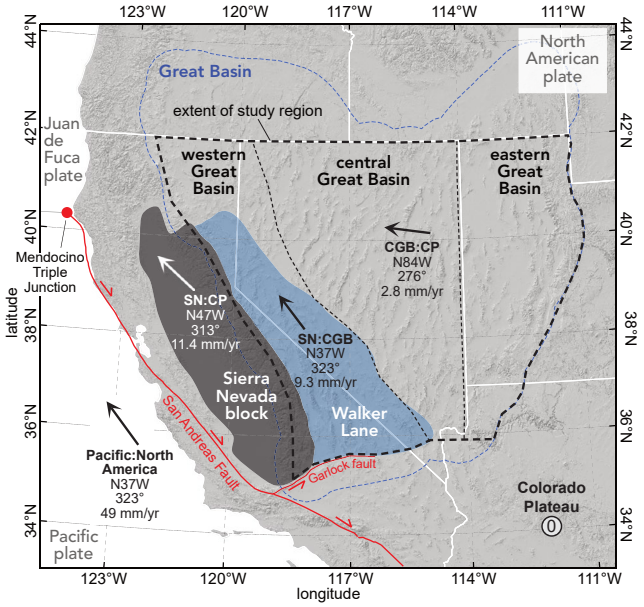

Figure 1. Map of tectonic provinces in the western U.S. with rates and orientations of relative motion from Bennett et al. (2003) based on GPS velocities. Western, central, and eastern Great Basin are defined based on Bennett et al. (2003) and our results. The boundary between the eastern and central regions of the Great Basin is an approximation. Orientations of motion relative to the Colorado Plateau are the same as relative to stable North America (Bennett et al., 2003; Dixon et al., 2000). Abbreviations: CP – Colorado Plateau; CBG – Central Great Basin; SN – Sierra Nevada. Walker Lane and Sierra Nevada block outlines are drafted after Stewart et al. (1988). The Great Basin outline is from the Nevada Bureau of Mines and Geology.

This debate over deformation style is ongoing in the western Great Basin (Walker Lane, blue area in Figure 1), a ~150-km-wide zone of transtension between the central Basin and Range province and the Sierra Nevada that accommodates ~15%–20% of Pacific-North America relative plate motion (Bennett et al., 2003; Bormann et al., 2016; DeMets & Merkouriev, 2016; Hammond et al., 2011; Lifton et al., 2013). When horizontal components of GPS velocities are used in block models to assign slip rates to faults that bound discrete blocks (Bormann et al., 2016; Evans et al., 2015, 2016; Hammond et al., 2011; Hammond & Thatcher, 2007; Meade & Hager, 2005), the model slip rates ("geodetic slip rates") are often inconsistent with fault slip rates determined by paleoseismic studies ("geologic slip rates"), even when the models include so many blocks that they approach a continuum (Evans et al., 2016). Similarly, where horizontal components of GPS velocities across a single fault or a transect of faults are different from geologic slip rates, the GPS velocities are often greater than the sum of the fault slip rates from paleoseismic studies, especially for strike-slip faults (Frankel et al., 2011; Gold et al., 2014; Lifton et al., 2013, 2015, 2020; Personius et al., 2017; Wesnousky et al., 2005). Where geologic and geodetic slip rates disagree, the mismatch may be accounted for by distributed deformation or missing earthquakes in the paleoseismic record (Dong et al., 2014; Frankel et al., 2011; Gold et al, 2013b, 2014; Lifton et al., 2013; Personius et al., 2017), vertical block rotations (Surpless & Kroeger, 2014; Wesnousky, 2005; Wesnousky et al., 2012), or temporal variations in fault slip rates (Angster et al., 2019; Gold, dePolo, et al., 2013a; Lifton et al., 2015). For normal faults, disagreement between geologically and geodetically measured horizontal components of rates may also result from conversion of vertical to horizontal components using an inaccurate fault dip (e.g., Friedrich et al., 2003; Personius et al., 2017).

It remains challenging to distinguish among the potential explanations for the mismatch in geologic and geodetic slip rates in the western Great Basin because these datasets characterize deformation over different spatial and temporal scales. GPS data span decades and can include transient responses to earthquakes in previous decades (e.g., Hammond et al., 2011; Kreemer, 2009), but Basin and Range faults commonly have earthquake recurrence intervals that exceed 1,000–10,000 years (e.g., Koehler & Wesnousky, 2011; Pérouse & Wernicke, 2017). Additionally, GPS stations in the Great Basin have denser spatial coverage than paleoseismic studies. Compounding the problem, nearby faults may trade off releasing strain (Angster et al., 2019; Gold, dePolo et al., 2013a), requiring regional paleoseismic analysis to develop a complete picture of strain accommodation. This mismatch in geologic and geodetic slip rates may be addressed by adding fault slip rates along transects to compare with GPS velocities for those areas (Koehler & Wesnousky, 2011; Personius et al., 2017; Wesnousky et al., 2005), but the most spatially complete picture of regional strain in the western U.S. is still from GPS velocity data (e.g., Kreemer, 2009). Recent syntheses of paleoseismic studies, however, now provide a relatively complete database of Holocene to Late Pleistocene fault slip rates in the northern Basin and Range province (Pérouse & Wernicke, 2017; Powers, 2020). Thus, it is now possible to compare strain on decadal and Holocene timescales across the Great Basin.

We use these databases to calculate horizontal components of velocity from fault slip rates for the entire Great Basin. We treat fault slip rates as analogous to seismic moments and sum them (England & Molnar, 1997; Kostrov, 1974; Molnar & Deng, 1984) to determine the pattern of average strain release and horizontal components of velocity over the past 15 Kyr while accounting for block rotations (Ekström & England, 1989; Haines, 1982; Haines & Holt, 1993; Holt et al., 1991). We then consider the fault-based results in context with horizontal GPS velocities and plate reconstructions to suggest a coherent history of strain release in the western Great Basin. Using this regional approach that spans decadal, Holocene, and Neogene datasets, we suggest that deformation in the western U.S. can be described as continuous deformation of a

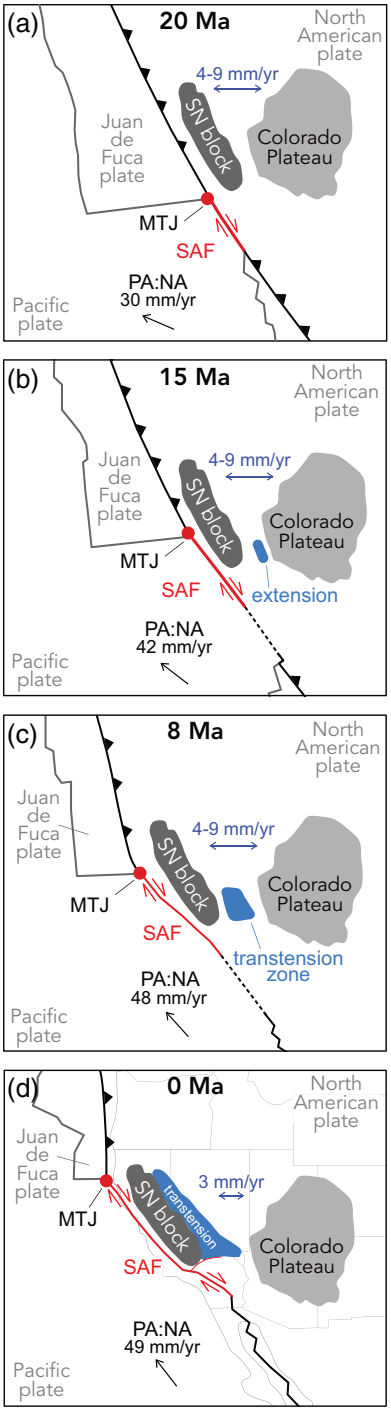

Figure 2. Conceptual illustration of the tectonic context of the western U.S. at (a) 20 Ma, (b) 15 Ma, (c) 8 Ma, and (d) present. The blue area highlights the growing zone of transtension in the western Great Basin as the Mendocino triple junction (MTJ) migrates north. SAF – San Andreas Fault; SN – Sierra Nevada. Figure inspired by Faulds and Henry (2008). Tectonic plate boundaries, MTJ locations, and SAF length are from Atwater and Stock (1998) and McQuarrie and Wernicke (2005). Pacific-North America plate (PA:NA) rates and orientations are from DeMets and Merkouriev (2016). Basin and Range extension rates prior to 0 Ma are from Sonder and Jones (1999) and references therein. Present day Basin and Range extension rate from Bennett et al. (2003).

thin viscous sheet with the Sierra Nevada block acting as a rigid boundary, and we assess the cause for the discrepancy in geologic and geodetic measurements of horizontal components of velocity in the Walker Lane.

2. Relevant Tectonic History

In the Great Basin north of present-day 37°N, extension initiated between 45 and 35 Ma and was widespread by ~25 Ma (Sonder & Jones, 1999; and references therein). In contrast, farther west at the same latitudes was a convergent margin with rapid subduction beneath western North America (Atwater, 1970; Atwater & Stock, 1998).

By ~28 Ma, the Pacific plate came into contact with the North American plate, forming the Mendocino triple junction at the junction of the Pacific, North American, and proto-Juan de Fuca plates (Atwater, 1970; Atwater & Stock, 1998; Sonder & Jones, 1999). From ~28 to 16 Ma (Figure 2a), dextral faulting replaced subduction south of the triple junction as the San Andreas Fault lengthened and the triple junction migrated northwest (Atwater, 1970; Atwater & Stock, 1998), and extension continued in the Great Basin north of present day 37°N (Sonder & Jones, 1999).

Between 18 and 16 Ma, the Mendocino triple junction migrated past the southern margin of the Sierra Nevada block (Atwater, 1970; Atwater & Stock, 1998; McQuarrie & Wernicke, 2005; DeMets & Merkouriev, 2016). Subsequently, a zone of transtension developed east of the Sierra Nevada block in the western Great Basin (e.g., Surpless et al., 2002). Extension began around 16–14 Ma in the western Great Basin south of present day ~37°N (Sonder & Jones, 1999; McQuarrie & Wernicke, 2005; Figure 2b), and dextral shear initiated around 13–12 Ma with the Las Vegas Valley shear zone and the Stateline fault (Faulds & Henry, 2008; Guest et al., 2007) and progressed northwestward (Busby, 2013; Faulds & Henry, 2008; McQuarrie & Wernicke, 2005; Wernicke & Snow, 1998). West of the Las Vegas Valley, dextral slip on the Death Valley-Fish Lake Valley fault system initiated ~10 Ma (Reheis & Sawyer, 1997), and farther north, shear in Dixie Valley likely began ~8 Ma (Colgan et al., 2020).

The period since ~13 Ma is also characterized by vertical axis rotation of crustal blocks in the western Great Basin. Rotation occurred at ~5°–6°/Myr from 13 to 3 Ma in the central Walker Lane (Carlson et al., 2013; Cashman & Fontaine, 2000; Grow, 2009; Petronis et al., 2009; Rood et al., 2011), but rotation was negligible in the northern Walker Lane near Pyramid lake (Cashman & Fontaine, 2000). In the southern Walker Lane near the Coso geothermal field, paleomagnetic studies yield rotation rates of ~4°/Myr since ~3 Ma on fault-bounded crustal blocks (Pluhar et al., 2006). Observations that rotation rates in younger rock elsewhere are slower (Cashman & Fontaine, 2000) and the modern strain field is incompatible with pre-3 Ma rotation rates (Hammond et al., 2011; Petronis et al., 2009) both suggest that vertical block rotations may play a more minor role today than they did before 3 Ma (Cashman & Fontaine, 2000; Grow, 2009; Hammond et al., 2011; Kreemer, 2009).

From ~17 Ma to present (Figure 2c), the San Andreas Fault lengthened, the triple junction migrated north, and the zone of transtension in the western Great Basin grew (Atwater & Stock, 1998; Faulds & Henry, 2008; McQuarrie & Wernicke, 2005; Sonder & Jones, 1999). The total dextral offset (cumulative displacement) since the onset of shear in the Walker

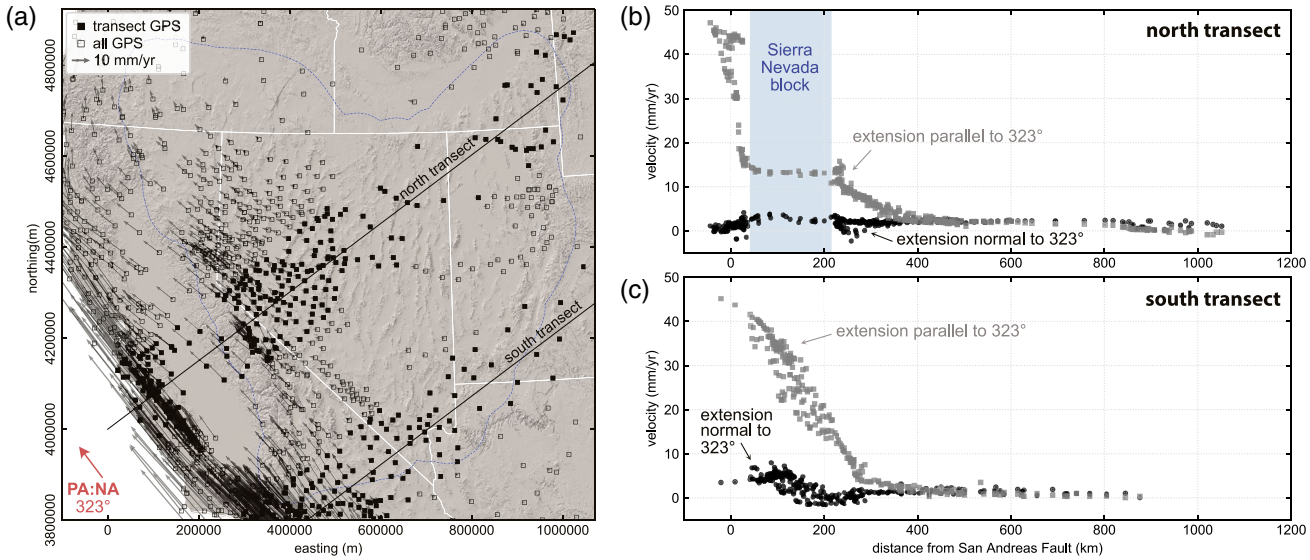

Figure 3. GPS velocities show the effectively rigid Sierra Nevada block within the deforming western U.S. continental lithosphere. (a) Map of GPS stations in the western U.S. from the MAGNET (Blewitt et al., 2018) and GAGE (Herring et al., 2016) databases. The extent of the Great Basin is approximated by the dashed line. Stations plotted with solid black squares are those used in the northern (b) and southern (c) transects, within 100 km of each transect center line. GPS velocities (b) across and (c) south of the Sierra Nevada block plotted as components parallel and normal to 323°, the orientation of relative motion between the Pacific and North American plates (Bennett et al., 2003; Dixon et al., 2000). The rigidity of the Sierra Nevada block is visible in the northern transect (b) at ~50–200 km from the San Andreas Fault.

Lane decreases from south to north (Faulds & Henry, 2008), as do GPS velocities across the Walker Lane (Bormann et al., 2016; Hammond et al., 2011; Lifton et al., 2013).

Today (Figures 1 and 2d), deformation within the Walker Lane accommodates ~15%–20% of the 49 mm/yr of relative motion between the Pacific and North American plates (Bennett et al., 2003; Bormann et al., 2016; DeMets & Merkouriev, 2016; Hammond et al., 2011; Lifton et al., 2013). GPS velocities (Figure 1) suggest a total displacement of 11.4 ± 0.3 mm/yr toward 313° between the Sierra Nevada block and the Colorado Plateau, consisting of 9.3 ± 0.2 mm/yr of displacement accommodated as right-lateral shear across the western Great Basin, parallel to Pacific-North America relative plate motion (323°), and ~2.8 ± 0.2 mm/yr of displacement accommodated by approximately east-west (276°) extension across the central and eastern Great Basin (Bennett et al., 2003).

Following Bennett et al. (2003), we subdivide the Great Basin into three sections (Figure 1) characterized by present-day deformation. The eastern Great Basin strains at a high rate in a zone that spans ~100 km, including the Wasatch Front. The central Great Basin strains slowly, and the western Great Basin (Walker Lane) is a zone of high transtensional strain rate (Figure 1, blue area) east of the Sierra Nevada and north of the Garlock fault. The Walker Lane (Locke et al., 1940; Stewart, 1980, 1988; Wesnousky, 2005) partly overlaps with the Eastern California Shear Zone as defined by Dokka and Travis (1990).

3. Methods

3.1. GPS Velocity Data

We used horizontal components of GPS velocities from the Geodesy Advancing Geosciences and EarthScope (GAGE; Herring et al., 2016) and Mobile Array of GPS for Nevada Transtension (MAGNET; Blewitt et al., 2018) continuous networks in a North-America-fixed reference frame (Figure 3). The GAGE dataset spans 1996–2019, and the MAGNET dataset spans 2004–2019. We calculated the total horizontal velocity from the north and east components, as well as the components of velocity parallel and normal to 313°, 317°, and 323°. We did not account for postseismic strain transients, but we did remove stations affected by magmatic processes in Long Valley Caldera. Figure 3 shows GPS velocities relative to the station's distance

from the San Andreas Fault along a transect oriented N53°E, normal to the direction of relative motion between the Pacific and North American plates (323°).

3.2. Strain from Fault Slip Rates

We calculated the contribution to strain by slip on individual faults in the Great Basin, north of the Garlock fault and south of 42°N, from two databases of fault slip rates (Pérouse & Wernicke, 2017; Powers, 2020; Figure 4). Slip rates are from Pérouse and Wernicke (2017) ("P&W faults"; Figures 4d–4f) and the 2018 update of the U.S. Geological Survey National Seismic Hazard Model ("USGS faults"; Figures 4a–4c, Petersen et al., 2020; Powers, 2020). We used the 15-ka time period following Pérouse and Wernicke (2017). Slip rates reported for normal faults in the USGS database are a mix of vertical components only and dip-slip rates (Powers, 2020). All vertical rates were converted to dip-slip rates prior to further analysis. Some fault slip rates in the USGS database may be estimated from a single earthquake in the Holocene, and therefore could be maximum rates. We used the reported geologic slip rates for the USGS faults (Figure 4a and Table S1). For the P&W database, if a fault lacked a slip rate for the 0–15 ka period but had a slip rate for the 0–80 ka period, we used the 0–80 ka slip rate, unless there is evidence that the fault was not active since 15 ka (Figure 4d and Table S2). We updated or added slip rates for the Pyramid Lake (Angster et al., 2016), Wassuk Range strike-slip (Dong et al., 2014), Benton Springs (Angster et al., 2019), and Indian Head faults (Angster et al., 2019) to both databases, for a total of 202 USGS faults and 107 P&W faults.

We used the 0–15 ka timescale because fault data are more complete for the past 15 Kyr than for longer time periods. The paleoseismic record is not complete enough to do the same analysis over a longer time span, and the fault databases are likely incomplete even on the 15-ka timescale. For example, the 2019 Ridgecrest earthquake ruptured both mapped and unmapped faults (Duross et al., 2020), and previously unidentified strike-slip faults have recently been reported in basins within the Walker Lane (Dong et al., 2014; Gold, Stephenson et al., 2013b). Additionally, many faults in the Great Basin are constrained by crosscutting shorelines from pluvial lake high stands that date to 12–15 ka (e.g., Hanks & Wallace, 1985).

To calculate the contribution to strain across the Great Basin from each fault, we calculated what is effectively a seismic moment rate tensor for each fault (e.g., England & Molnar, 1997, 2005; Molnar & Deng, 1984; Molnar 1983), and then added them cumulatively across the Great Basin (Figures 5 and 6a). We first calculated the north (M_{nn}), east (M_{ee}), and shear (M_{en}) components of the moment tensor for slip on each fault according to the equations (Aki & Richards, 2002):

$$M_{ee}^{x} = \dot{M}_o\left(\sin\delta\cos\lambda\sin 2\phi - \sin 2\delta\sin\lambda\cos^2\phi\right) \tag{1}$$

$$M_{nn}^{x} = -\dot{M}_o\left(\sin\delta\cos\lambda\sin 2\phi + \sin 2\delta\sin\lambda\sin^2\phi\right) \tag{2}$$

$$M_{en}^{x} = \dot{M}_o\left(\sin\delta\cos\lambda\cos 2\phi + \frac{1}{2}\sin 2\delta\sin\lambda\sin^2\phi\right) \tag{3}$$

Where x indicates each fault, e and n are east and north directions, δ is fault dip, ϕ is fault strike, and λ is fault rake. Seismic moment rate, $\dot{M}_o$, for each fault is (Aki & Richards, 2002):

$$\dot{M}_o = \frac{\mu \times h \times \text{fault length} \times \text{slip rate}}{\sin\delta} \tag{4}$$

Where μ is shear modulus and h is depth of the seismogenic crust. Because we consider depth to the base of the seismogenic crust, h, and shear modulus, μ, to be constant for faults in this analysis, the only variables in the moment tensor are fault length (m), slip rate (m/yr), and orientations (strike, dip, and rake) of the faults. We assume 90° dip for strike-slip faults and 50° dip for normal faults. Rake is 180° for dextral faults, 0° for sinistral faults, and −90° for normal faults. We calculated strike for each fault based on the endpoints and midpoint of the line segment because strike is not reported in either fault database. We then calculated the contribution of each fault, x, to the strain rate tensor in units of yr^{-1} according to (Kostrov, 1974):

10.1029/2020TC006389

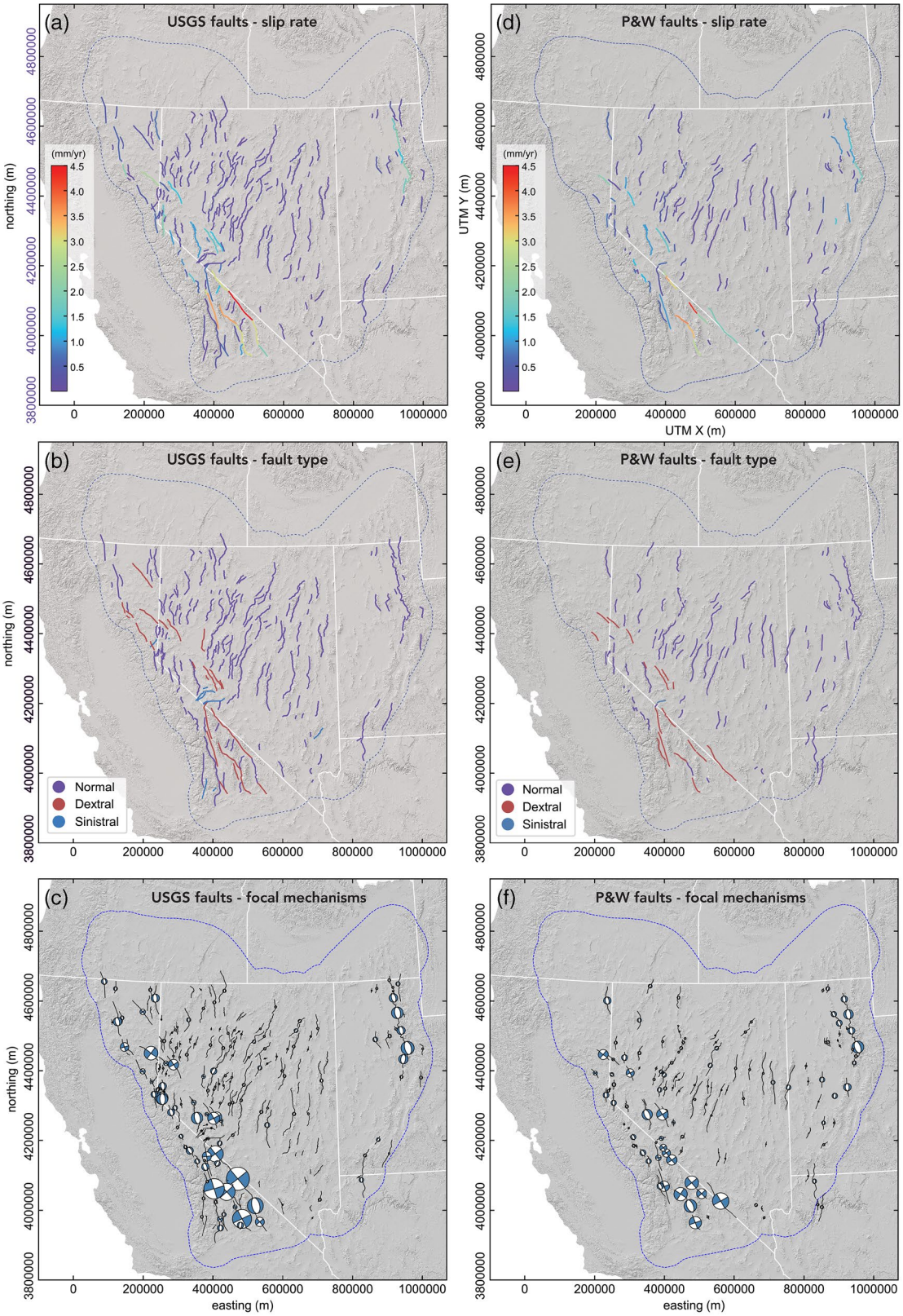

Figure 4. Fault data used in this analysis from (a)–(c) the USGS National Seismic Hazard Model source faults database (Petersen et al., 2020; Powers, 2020) and (d)–(f) the Pérouse and Wernicke (2017) neotectonic database. The lower hemisphere stereographic projections of focal mechanisms in (c) and (f) represent fault kinematics and radii are scaled by the product of slip rate and fault length. The extent of the Great Basin is shown with a blue dashed outline.

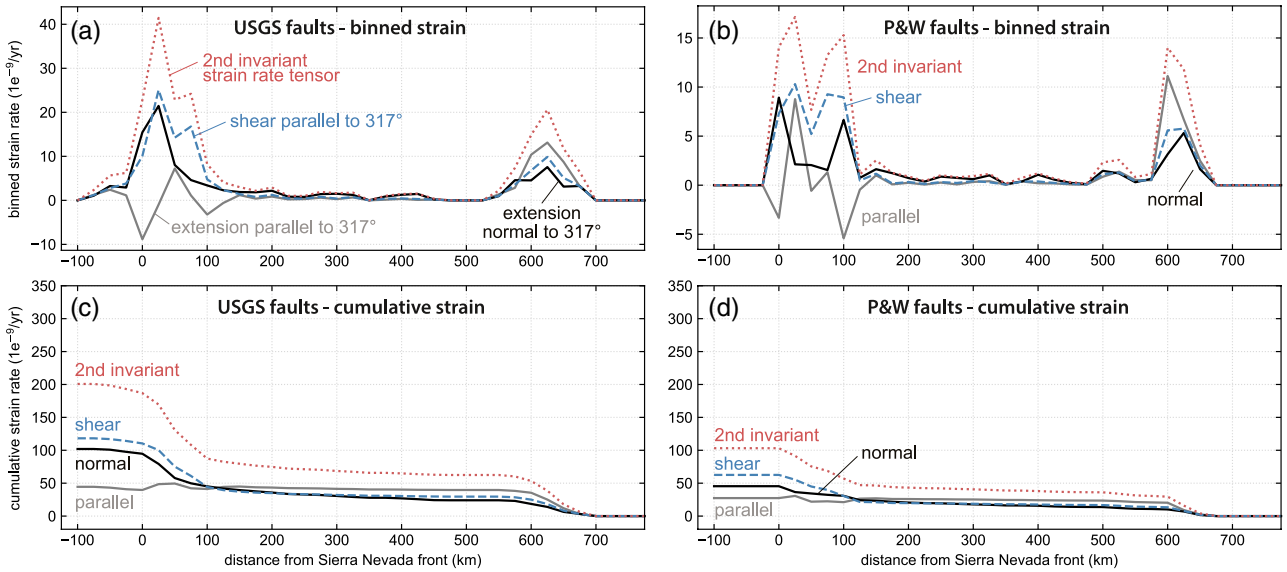

Figure 5. The contribution to strain by slip on faults in the Great Basin calculated from the USGS National Seismic Hazard Model source faults (Petersen et al., 2020; Powers, 2020) and the Pérouse and Wernicke (2017) database. Strain components are calculated in 25-km-wide swaths (a)–(b) and plotted cumulatively from east to west (c)–(d) relative to 317°. The contribution to strain by slip on each fault is show in components of extension parallel to 317° ("parallel"), extension normal to 317° ("normal"), and shear parallel to 317° ("shear").

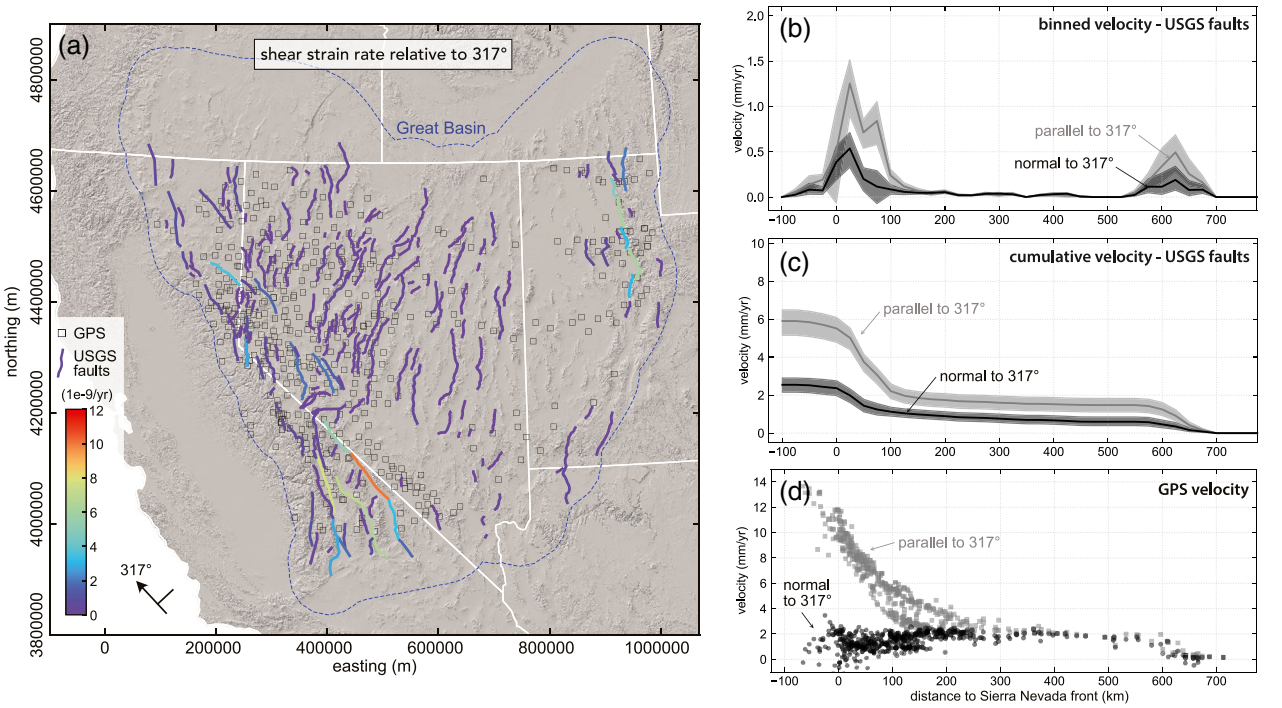

Figure 6. (a) Map of the western U.S. with the USGS faults colored by their contribution to average shear strain within the Great Basin. Open squares are GPS station locations. Components of velocity parallel and normal to 317°, and relative to North America, calculated from the USGS faults (b) in 25-km-wide swaths and (c) added cumulatively. (d) GPS velocity components parallel and normal to 317° in a North-America-fixed reference frame.

$$\dot{\varepsilon}_{ij}^{x} = \frac{\dot{M}_{ij}^{x}}{2\mu h A} \tag{5}$$

where A is the area (m^2) of the region containing the faults, where we used 25-km-wide swaths (Figures S1 and S2) parallel to θ, the orientation of interest. Note that neither μ nor h enters, because they are factors in the numerator of the seismic moments. We rotate the strain rate tensor to get the components of strain relative to different orientations according to the rotation matrix:

$$\begin{Bmatrix} \dot{\varepsilon}_{\text{normal}}^{x} \\ \dot{\varepsilon}_{\text{parallel}}^{x} \\ \dot{\varepsilon}_{\text{shear}}^{x} \end{Bmatrix} = \begin{bmatrix} \cos^2\theta & \sin^2\theta & 2\sin\theta\cos\theta \\ \sin^2\theta & \cos^2\theta & -2\sin\theta\cos\theta \\ -\sin\theta\cos\theta & \sin\theta\cos\theta & \cos^2\theta - \sin^2\theta \end{bmatrix} \begin{Bmatrix} \dot{\varepsilon}_{ee}^{x} \\ \dot{\varepsilon}_{nn}^{x} \\ \dot{\varepsilon}_{en}^{x} \end{Bmatrix} \tag{6}$$

And the components of the strain rate tensor for each fault are:

$$\dot{\varepsilon}_{\text{normal}}^{x} = \dot{\varepsilon}_{ee}^{x}\cos^2\theta + \dot{\varepsilon}_{nn}^{x}\sin^2\theta + 2\varepsilon_{en}^{x}\sin\theta\cos\theta \tag{7}$$

$$\dot{\varepsilon}_{\text{parallel}}^{x} = \varepsilon_{ee}^{x}\sin^2\theta + \varepsilon_{nn}^{x}\cos^2\theta - 2\varepsilon_{en}^{x}\sin\theta\cos\theta \tag{8}$$

$$\dot{\varepsilon}_{\text{shear}}^{x} = \left(\varepsilon_{nn}^{x} - \varepsilon_{ee}^{x}\right)\sin\theta\cos\theta + \varepsilon_{en}^{x}\left(\cos^2\theta - \sin^2\theta\right) \tag{9}$$

where θ is the angle of rotation. We calculated strain components relative to orientations between 310 and 325° to span the orientations of relative motion between the Sierra Nevada block and the Colorado Plateau (313°) and the Pacific and North American plates (323°; Bennett et al., 2003; Dixon et al., 2000) and to determine the orientation along which extension is minimized.

Finally, we calculated the distance from each fault centroid to the Sierra Nevada front along a transect oriented normal to the orientation of interest (Figure S3) and summed the contribution to strain from each fault in 25-km-wide swaths according to:

$$\dot{\varepsilon}_{ij} = \sum_{x} \dot{\varepsilon}_{ij}^{x} \tag{10}$$

We also calculated a second invariant of the strain rate tensor, $\dot{E}$, following the definition used by Kreemer et al. (2014):

$$\dot{E} = \sqrt{{\dot{\varepsilon}_{\text{normal}}^{x}}^2 + {\dot{\varepsilon}_{\text{parallel}}^{x}}^2 + 2{\dot{\varepsilon}_{\text{shear}}^{x}}^2} \tag{11}$$

3.3. Velocity from Strain Rate

To convert average regional strain rate to horizontal velocity in mm/yr (Figures 6b and 6c), we followed the method of Haines (1982), who demonstrated that when both the strain rates within a region and the velocity along an edge are known, velocities within the deforming region can be calculated despite ignorance of the vorticity field or the complete velocity gradient tensor (Haines, 1982, see also: Ekström & England, 1989; Haines & Holt, 1993; Holt et al., 1991; Jackson & McKenzie, 1988; McKenzie & Jackson, 1983). In most applications, a boundary is rigid, and velocities are computed relative to that rigid boundary. From the calculation of components strain rates for each 25-km-wide swath, we found the orientation that minimizes extension parallel to the length of the swaths, $\dot{\varepsilon}_{\text{parallel}}$, so that we can assume no extension parallel to the swaths. Defining "parallel" as the x-direction in Haines (1982) formulation (and the long direction for each swath), $\dot{\varepsilon}_{\text{parallel}} = \frac{\partial u}{\partial x} = 0$. Moreover, with no movement along the x-direction at the boundary, $v = 0$, and

therefore, $\frac{\partial v}{\partial x} = 0$. Thus, the velocity field in a one-dimensional transect can be solved by integrating the components of strain rate over y. We find that, on average across the central and western Great Basin, the component of extension parallel 317° is zero (Figure 5c). Velocity is calculated across each swath by treating the southeast edge of the swath as fixed so that the difference in velocity across each swath is equal to the strain across the swath times the swath width, w, 25 km. Thus:

$$\dot{\varepsilon}_{\text{normal}} = \frac{\partial v}{\partial y} = \frac{V_{\text{normal}}}{w} \tag{12}$$

$$\dot{\varepsilon}_{\text{shear}} = \frac{1}{2}\left[\frac{\partial v}{\partial x} + \frac{\partial u}{\partial y}\right] = \frac{1}{2}\left[\frac{\partial u}{\partial y}\right] = \frac{1}{2}\frac{V_{\text{parallel}}}{w} \tag{13}$$

And velocity in each swath is:

$$\begin{aligned} V_{\text{normal}} &= \dot{\varepsilon}_{\text{normal}} \times w \\ V_{\text{parallel}} &= 2\dot{\varepsilon}_{\text{shear}} \times w \end{aligned} \tag{14}$$

This method accounts for rotations about vertical axes in the velocity calculation. Since the entire Great Basin is included in the analysis, rotations of blocks within the Walker Lane are implicit in the velocity field calculation.

3.4. Limitations

The primary limitation to this analysis is the assumption that there is no extension parallel to the length of each 25-km-wide swath. Although the assumption is valid when averaged across the central and western Great Basin (Figures 5a and S8), it is not valid in the eastern Great Basin. A more northerly orientation is required to minimize the parallel component of strain across the eastern Great Basin (Figure 5a). As this region is not the focus of our study, we ignore this shortfall of the approach. Similarly, the strain-rate calculations show the assumption is valid as an average across the entire western Great Basin, but split into northwest, central, and southeast sections, a single orientation does not satisfy all regions. Analyzed in sections, strain and velocity are highest for the southeast region and decrease to the northwest, confirming prior observations from GPS data (Bormann et al., 2016; Hammond et al., 2011; Lifton et al., 2013). The assumption remains valid for the regional average velocity presented herein.

3.5. Sensitivity Analysis

To assess sensitivity of the strain and velocity calculations to the source fault parameters (strike, dip, and slip rate), cumulative strain and velocity were calculated 10,000 times using values randomly selected from a normal distribution for each parameter (Figures 7, S4, and S5). The bounds are ±15° for dips of normal faults, ±10° for dips of strike-slip faults, ±10° for strikes, and ±30% for slip rates. We use ±10° for strike because strike is not reported in either database; we calculate strike for each fault from the endpoints and midpoint of the fault. We use ±30% for slip rate because slip rate is most uncertain of all the input parameters (e.g., dePolo & Anderson, 2000; Stein & Friedrich, 2014). For example, faults with 0.5 mm/yr slip rates (7.5 m offset in 15 Kyr) and recurrence intervals of 5 Kyr are comparably likely to have offsets of 5 or 10 m in an arbitrary 15-Kyr period, which is consistent with a 30% uncertainty in rates estimated from faulting since 15 ka. Strike, dip, and slip rate (Figures 7a–7c) all contribute to total uncertainty (Figure 7d), with dip having the smallest effect. If all of the normal faults slipped on low-angle (35°) fault planes, however, the normal component of horizontal velocity associated with extension would be at the upper end of the range shown in Figure 7b (~3 mm/yr). At the western edge of the study region, there is +10/−13% (+0.6/−0.8 mm/yr) uncertainty in the component of velocity parallel to 317° and ±15% (0.4 mm/yr) uncertainty in the component of velocity normal to 317°.

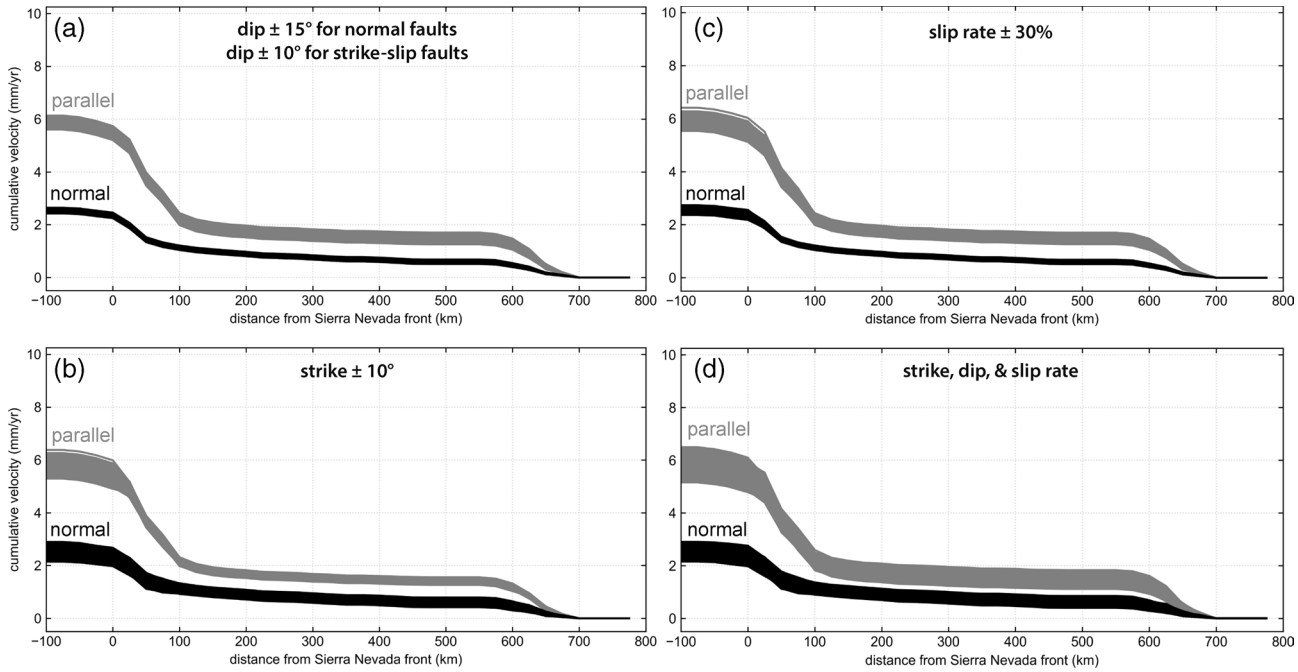

Figure 7. Sensitivity analysis showing how the components of velocity parallel and normal to 317° are affected by variation in (a) normal fault dip of ±15° and strike-slip fault dip of ±10°, (b) fault strike of ±10°, and (c) slip rate of ±30%. (d) The result of allowing all of strike, dip, and slip rate to vary. Ranges are shown for 10,000 calculations with random values chosen from normal distributions of each parameter for each fault (Figure S1).

Swath dimensions and orientation may also affect the results. Calculated strain rates scale linearly with swath length, but uncertainty in length is small because we calculate the length of each swath individually (Figure S2). Assumed swath widths between 5 and 50 km have no effect on the velocity results (Figure S6). Over the 15° -range (310–325°) for which we calculated strain and velocity, the parallel component of velocity varies by ±1 mm/yr and the normal component of velocity varies by ±0.5 mm/yr (Figure S7).

4. Results

Strain rates across the Great Basin calculated from the USGS (Petersen et al., 2020; Powers, 2020) and Pérouse and Wernicke (2017) databases of 15-ka fault slip rates reveal similar patterns (Figures 5 and 6a, Tables S1 and S2). Both datasets show zones of higher strain rate in the east and west with lower rates across the central Great Basin in a coordinate system relative to 317° (N43°W; Figures 5a and 5b). The eastern zone of high strain is ~100-km-wide and spans the Wasatch fault zone and smaller faults east and west of it. In the central Great Basin, extension parallel to 317° is zero, and shear parallel to 317° and extension normal to 317° are low for both datasets. In the western Great Basin, a zone spanning ~150 km from the Sierra Nevada front, shear parallel to 317° and extension normal to 317° dominate, while extension parallel to 317° averages to nearly zero across the region (Figures 5c and 5d). Though the USGS and P&W datasets reveal similar patterns of strain release over the past 15 Kyr, cumulative strain rate for the P&W fault database is lower by nearly half (Figures 5c and 5d) because that database contains fewer faults than the USGS database. Despite the large difference in cumulative strain rate between the two datasets, they document similar rates across the eastern Great Basin. The remainder of this study focuses on results from the USGS faults database because it contains more faults and slip rates (Figure 4).

Across the Great Basin, the cumulative sum of strain rates calculated from faults in the USGS database (Figure 5c) yields velocities relative to stable North America (Figures 6b and 6c) between opposite sides of the Great Basin with ~6 mm/yr in the component parallel to 317° and ~2.5 mm/yr in the component normal to 317° (parallel to 47°). The majority of both components of velocity are accommodated in a zone

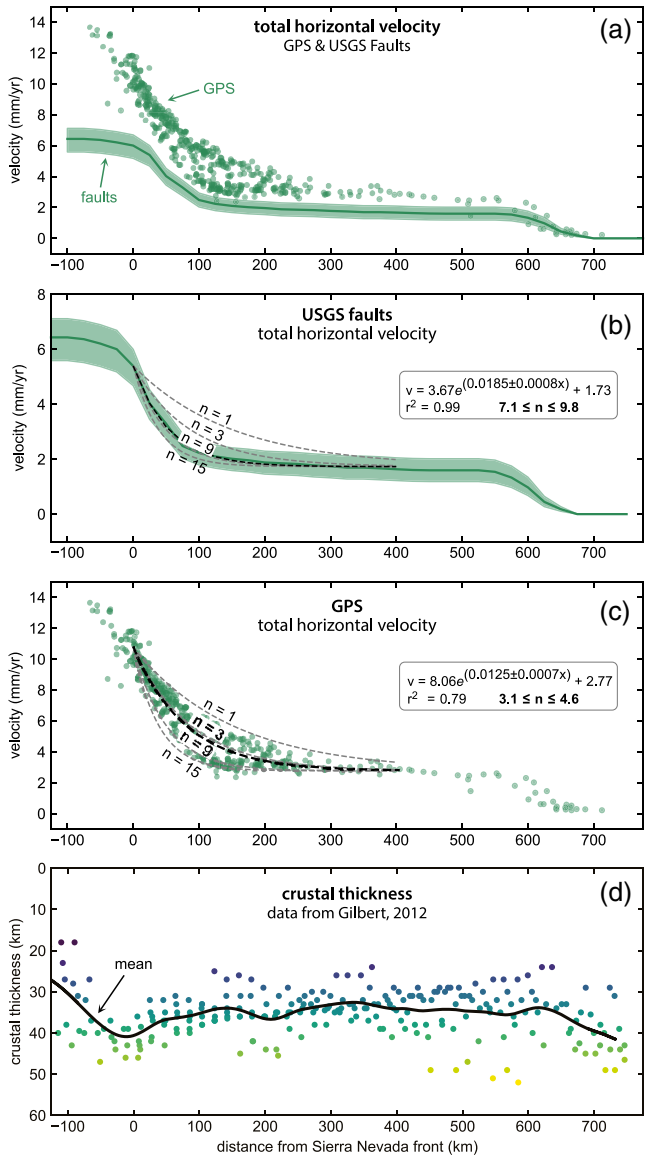

Figure 8. (a) Total horizontal velocity from GPS and fault data across the Great Basin. Both datasets are the square root of the sum of the squares of the two horizontal components of velocity. Locations of GPS stations are shown in Figure 6a. (b) Fault and (c) GPS velocity fields with velocities (mm/yr) calculated for different values of n, the exponent that relates strain rate ($\dot{\varepsilon}$) to stress (τ) by $\dot{\varepsilon} \sim \tau^n$. Best fit curves (black dashed lines) yield $n \approx 9$ and $n \approx 4$ for fault and GPS data, respectively. We calculate n from the boxcar-shaped tangential boundary condition where $\lambda = \frac{\text{length of boundary}}{4\sqrt{n}}$ (Whitehouse et al., 2005) and λ is the reciprocal of the exponent in the best-fit curve (e.g., $\lambda = \frac{1}{0.0185} = 54$ km for the fault velocity field). We report ranges of n for the fault and GPS datasets calculated using 600–645 km for the length of the Sierra Nevada and the uncertainty in each exponent. (d) Crustal thickness from EarthScope USArray seismic station data (Gilbert, 2012). See Figure S10 for a map of these data.

~150 km wide in the western Great Basin, the Walker Lane, with ~4 mm/yr parallel to 317° and ~1.5 mm/yr normal to 317°.

5. Discussion

5.1. Geologic Versus Geodetic Velocity Fields

The velocity fields calculated from geologic and geodetic data across the Great Basin show similar patterns of regional velocity but differ in magnitude (Figures 6 and 8). Both datasets show regions of faster straining in the east and west, with slower straining across the central Great Basin (Figures 6b–6d). Considering the total horizontal velocity relative to stable North America, the results from geologic and geodetic data are within uncertainty in the eastern Great Basin, within 1 mm/yr across the central Great Basin, and diverge in the western Great Basin, where the majority of shear and extension concentrate within ~150 km of the Sierra Nevada front (Figure 8a).

Across the central and eastern Great Basin, our results show total horizontal velocity of ~2.4 mm/yr, and GPS finds 2.8 mm/yr (Figure 8; Bennett et al., 2003). The datasets and prior studies agree that most of the strain is accommodated along the eastern margin of the Great Basin with low but measurable deformation rates across the central Great Basin over the past 15 Kyr (Figure 6b; Bennett et al., 2003; Hammond et al., 2014; Koehler & Wesnousky, 2011).

Across the western Great Basin, the horizontal component of the velocity field derived from fault data increases by 4 mm/yr, and the velocity field from GPS data increases by ~7–10 mm/yr (Figure 8a; Bennett et al., 2003; Hammond et al., 2011; Lifton et al., 2013; Bormann et al., 2016). In the western Great Basin (Walker Lane), the average 4 mm/yr rate from faults and 9.3 mm/yr rate from GPS (Bennett et al., 2003) hide a north-south gradient in velocity (Figure S8). GPS measurements show 7 mm/yr accommodated across the northern Walker Lane (Hammond et al., 2011), 8 mm/yr in the central (Bormann et al., 2016), and nearly 10 mm/yr in the south (Lifton et al., 2013). Our results show the same southward increase, from ~12.5% of the velocity accommodated north of 40°N and ~62.5% of the velocity accommodated south 38°N (Figure S8).

The majority of the difference in fault-derived versus GPS velocity fields is in the component of velocity parallel to 317°. The fault data show a small fraction of velocity parallel to 317°, with the parallel component of velocity more than double the magnitude of the normal component of velocity at the western end of the study region (Figures 6b and 6c). For the GPS data, the parallel component of velocity is 6–7 times the magnitude of the normal component of velocity (Figure 6d).

Despite the difference in magnitude and relative proportion of velocity components, the orientation of maximum shear is similar for fault-derived and GPS velocity fields. The orientation of maximum shear in the western Great Basin is 317° calculated from the USGS faults database, which is 6° different from the 323° orientation calculated from GPS data (Bennett et al., 2003). The 6° difference in orientation is within error of the fault strike calculation (Figures S4 and S5), and faults may be slightly misoriented relative to the current orientation of maximum strain.

In summary, the velocity fields calculated from geologic and geodetic sources within the Great Basin agree in shape and orientation while differing in proportion and magnitude. The majority of shear and extension concentrates in the western Great Basin (Walker Lane), but the amount and relative proportion of shear is lower for the fault-derived velocity field than for the GPS velocity field. The similarity between the GPS and fault-derived velocity fields suggests that the pattern of strain release in the Great Basin has been consistent over the past 15 Kyr, while the disagreement in proportion and magnitude suggests that evidence of shear is missing from the geologic record in the western Great Basin.

5.2. Implications for Missing Shear in the Walker Lane

As discussed earlier, prior studies have documented a similar mismatch between geologic and geodetic slip rates in parts of the Walker Lane (Frankel et al., 2011; Gold et al., 2014; Lifton et al., 2013, 2015, 2020; Personius et al., 2017; Wesnousky et al., 2005) and suggest that the difference in rates could be due to a combination of distributed deformation that occurs off major faults or missing earthquakes in the paleoseismic record (Dong et al., 2014; Frankel et al., 2011; Gold et al, 2013b, 2014; Lifton et al., 2013; Personius et al., 2017), vertical block rotations (Surpless and Kroeger, 2014; Wesnousky, 2005; Wesnousky et al., 2012), or temporal variations in fault slip rates (Angster et al., 2019; Gold, dePolo, et al., 2013a; Lifton et al., 2015).

Our analysis corroborates the deficit of shear documented in the paleoseismic record. However, because the velocity field calculated from fault data includes rotations (Haines, 1982; Ekström & England, 1989), if the difference in velocity calculated from geologic versus geodetic data were due to hidden, unobserved rotations of blocks about vertical axes, those rotations would require slip on faults that have been overlooked or whose rates have been underestimated. Paleomagnetic declinations document 5°/Myr rotation rates since 13–9 Ma in parts of the central and northern Walker Lane (Cashman & Fontaine, 2000; Petronis et al., 2009; Rood et al., 2011), but some studies also suggest that rotation rates have decreased since 3 Ma (Cashman & Fontaine, 2000; Petronis et al., 2009). Though modern rotation rates may be minor (1°–2°/Myr) as compared to rotation rates prior to 3 Ma (Figure S9; Bormann et al., 2016; Hammond et al., 2011; Kreemer, 2009), vertical axis rotations of crustal blocks still play a role in accommodating strain within the Walker Lane (Carlson et al., 2013; Grow, 2009; Oldow et al., 2008; Pluhar et al., 2006). Since vertical block rotations are often accommodated by slip on many small, discontinuous faults, some of which slip obliquely (Oldow et al., 2008; Pluhar et al., 2006), it may be difficult to measure fault slip rates on the faults that can accommodate the required strain and rotation.

The regional approach to calculating the velocity field from fault slip rates also allows us to discard transient fault strain rates as a potential reason for the disagreement in slip rates. Relative motion between the Pacific and North American plates has been constant in rate and orientation since at least 8 Ma (Atwater & Stock, 1998; DeMets & Merkouriev, 2016), and we consider the entire Walker Lane rather than a transect at a particular latitude. It is therefore unlikely that transient fault strain rates affect the entire studied region. More likely explanations for the lack of shear in the geologic record is that shear is (a) accommodated on unknown strike-slip faults, (b) accommodated by oblique slip on dominantly normal faults, (c) accommodated as permanent distributed deformation lost to the paleoseismic record, (d) underestimated by field measurements of lateral offsets on strike-slip faults, (e) released in moderate magnitude earthquakes on known faults that are mostly invisible in the paleoseismic record, or a combination of the above.

The paleoseismic record may suffer from a selection bias toward overrepresentation of normal faults as compared to strike-slip faults. Normal fault scarps are often more obvious in a landscape, with offset that is more easily recognized and measured, than strike-slip fault scarps. For example, Dong et al. (2014) reported a previously unknown strike-slip fault in the basin adjacent to the Wassuk Range normal fault, and Gold, Stephenson et al. (2013b) reported a previously unidentified strike-slip fault in Grizzly Valley, northern Walker Lane. Unknown strike-slip faults may pervade the Walker Lane, as the 2019 Ridgecrest earthquake also demonstrated when it ruptured both mapped and unmapped faults (Duross et al., 2020). Furthermore, evidence of vertical displacement, especially small magnitude, is more likely to remain visible in a landscape after an earthquake than is evidence of lateral displacement, because small lateral offsets may be subtle or may be easily erased by landscape change, especially if faulting is partitioned such that strike-slip

components are more common in basins than in surrounding terrain (Dong et al., 2014; Gold, Stephenson et al., 2013b).

Second, missing shear may be accommodated on oblique-slip faults with complex rupture patterns, such as those that accommodate vertical axis rotations (e.g., Oldow et al., 2008; Pluhar et al., 2006), including dominantly normal faults with a component of lateral displacement. Many historical Basin and Range earthquakes have minor components of strike-slip displacement that could be hard to recognize many years after an earthquake. For example, 17 cm of lateral slip on the Lost River fault in the 1983 Borah Peak earthquake amounted to 17% of the total slip (Crone et al., 1987). In the 1954 Dixie Valley-Fairview Peak earthquake sequence, both vertical and lateral slip occurred on the Fairview Peak fault, and lateral slip was also accommodated on three minor fault traces (Caskey et al., 1996).

Missing shear may be accommodated as off-fault permanent deformation in wide damage zones, making measurements of lateral offset more likely to underestimate displacement. Recent studies documenting offsets after large strike-slip earthquakes in Pakistan and southern California suggest that 30%–45% of slip may be accommodated off the primary fault (Gold et al., 2015; Milliner et al., 2016), which is difficult to measure in the field and may not be evident in a paleoseismic trench or in the landscape years after an earthquake. Major earthquakes in eastern Asia commonly include deformation spanning regions tens of kilometers in width along faults zones 100 km or more in length, like the 1889 Chilik earthquake in Kyrgyzstan (Abdrakhmatov et al., 2016), the 1905 Bulnay earthquakes in northern Mongolia (e.g., Baljinnyam et al., 1993; Choi et al., 2018), and the 1957 Gobi-Altay earthquake (Florensov & Solonenko, 1963; Kurushin et al., 1997). Furthermore, numerical models of landscape evolution suggest that strike-slip offsets in wide fault zones underestimate modeled slip, as do offsets measured many years after an earthquake (Reitman et al., 2019).

Finally, the 2020 Monte Cristo, Nevada, earthquake is modern evidence of a moderate earthquake producing oblique slip that may be missed in the paleoseismic record. The M6.5 earthquake reached a peak slip of 0.8 m at 4 km depth and produced only small surface offsets up to ~20 cm (Koehler et al., 2021; Zheng et al., 2020), with most offsets <5 cm and distributed in zones up to 800 m wide (Koehler et al., 2021). Small offsets are hard to measure in the field, will be quickly eroded on the surface, and may be concealed by displacement from larger earthquakes in a paleoseismic trench. The earthquake is near the upper range in magnitude of earthquakes that are unlikely to produce surface rupture (dePolo, 1994) but can accommodate shear. If shear is accommodated by more frequent M6.5 earthquakes than by fewer, larger earthquakes, it is not surprising that the paleoseismic record is missing evidence of shear. Additionally, if small blocks rotate around vertical axes, they must be bounded by minor faults. Since small faults are more likely have very long recurrence intervals and slip in moderate magnitude earthquakes, the record of slip due to block rotations may be hidden from the paleoseismic record.

In summary, multiple mechanisms that contribute to underrepresentation of shear in the geologic record may explain the mismatch between geologic and geodetic deformation rates and styles across the Walker Lane. Missing strike-slip faults and earthquakes, underestimation of strike-slip offsets, and distributed permanent deformation together likely account for the observed deficiency in geologic evidence of shear across the Walker Lane.

5.3. Strain Concentration in the Walker Lane

The observed concentration of strain in the Walker Lane can be explained by shear along the San Andreas fault, the existence of the Sierra Nevada block, rheology of continental lithosphere, and the tectonic history of western North America. England et al. (1985) demonstrated that the length scale of deformation in a homogenous thin viscous sheet with a moving boundary on one side depends on the type of boundary and rheology of the viscous sheet (lithosphere). When the velocity is tangential to the boundary (strike-slip), the length scale of deformation within the viscous layer is approximately four times smaller than when the velocity is normal (extension or compression) to the boundary. The e-folding length scale of deformation (λ) for velocity tangential to the boundary scales by $\lambda = \frac{L}{4\sqrt{n}}$, where n is the exponent that relates strain rate ($\dot{\varepsilon}$) to stress (τ) by $\dot{\varepsilon} \sim \tau^n$ and L is the length of the boundary (England et al., 1985; Whitehouse et al., 2005).

For an indenting boundary, the relationship is $\lambda = \frac{L}{\sqrt{n}}$ (England et al., 1985; Whitehouse et al., 2005). The 4x scaling holds independent of the value of n. Higher values of n result in strain concentrating closer to the boundary, assuming a homogenous lithosphere.

The western U.S., however, does not have homogenous lithosphere. The Sierra Nevada block occupies ~200 km between the San Andreas Fault and the western Great Basin and behaves more rigidly than the surrounding lithosphere. The relative rigidity of the Sierra Nevada is evident in the decay of GPS velocities in a San Andreas Fault-parallel coordinate system (Figure 3; Whitehouse et al., 2005). Whitehouse et al. (2005) modeled the decay of GPS velocities from the San Andreas Fault in the cases of a homogenous lithosphere and a lithosphere with a rigid block inclusion approximating the Sierra Nevada dimensions and relative velocity, which is oriented 10° more west than the motion of the Pacific plate relative to North America (Bennett et al., 2003). Whitehouse et al. (2005) found $n \approx 3$ best approximates GPS velocities both with and without a rigid block inclusion, demonstrating both the nonlinearity of the lithospheric rheology and the relative rigidity of the Sierra Nevada block.

Due to its relative rigidity and unique orientation, the Sierra Nevada block acts as a shear boundary for the western Great Basin. Consequently, part of the Pacific-North America relative movement is transferred across the block and into the Walker Lane (Kreemer, 2009; Whitehouse et al., 2005). The strain transfer is illustrated by transects of GPS velocities across the Sierra Nevada and south of it (Figure 3). In a plate-boundary parallel orientation (323°), as much as 25% of the 49 mm/yr of Pacific-North America relative plate motion is taken up east of the Sierra Nevada block (Figure 3). At 300 km from the San Andreas fault, velocity east of the Sierra Nevada block is ~7 mm/yr (Figure 3b), but in a transect south of the Sierra Nevada, velocity is only ~4 mm/yr at the same distance (Figure 3c).

Using these GPS data and our fault-derived velocity field, we estimate n for the Great Basin lithosphere from the Sierra Nevada boundary. For the fault-derived velocity field, we find $n \approx 9$ provides the best fit to the data, with a total range within uncertainty of $7 \leq n \leq 10$ (Figure 8b). For the GPS velocity field east of the Sierra Nevada, we find that $n \approx 4$ provides the best fit to the data, with a total range within uncertainty of $3 \leq n \leq 5$ (Figure 8c). The value of n from GPS dataset is similar to the results of Whitehouse et al., (2005), but the value of n from the fault data is higher. For a tangential boundary, strain concentrates ~40% closer to the boundary for $n = 9$ than for $n = 3$ and 67% closer to the boundary for $n = 9$ than for a medium with a linear rheology ($n = 1$; England et al., 1985; Whitehouse et al., 2005). The higher value of n that we obtain from fault data than the GPS data suggests that strain may have concentrated closer to the western edge of the Sierra Nevada block over the past 15 Kyr than it has over the past few decades. We suspect that the more widespread deformation in the GPS data may result from transient movements diffusing away from earthquake ruptures in central Nevada from 1915 to 1954, before GPS control points were installed (e.g., Hammond et al., 2011; Kreemer, 2009). The values of $n > 5$ also suggest that processes besides dislocation creep of typical rock forming minerals, such as frictional resistance to slip on faults, limit deformation of the lithosphere beneath the Basin and Range province (Sonder & England, 1986).

The observed 15-ka-to-present strain concentration in the Walker Lane has not existed since the onset of Basin and Range extension (e.g., Pérouse & Wernicke, 2017). Present-day crustal thickness is nearly constant across the Great Basin (Figure 8d; Gilbert, 2012; Long, 2019), which would not be possible if modern strain rates were extrapolated back to the onset of extension in the Basin and Range between 35 and 45 Ma. Instead, widespread crustal extension and thinning of a higher Great Basin was the primary deformation style prior to the mid-Miocene (~16 Ma; Bahadori et al., 2018; Long, 2019; Sonder & Jones, 1999). Since ~16 Ma, however, shear at the western margin of the North America plate and from the motion of the Sierra Nevada block relative to the Great Basin have had a larger influence on deformation style in the western Great Basin (Bahadori & Holt, 2019; Kreemer, 2009; McQuarrie & Wernicke, 2005; Parsons & Thatcher, 2011).

This shift occurred after the Mendocino triple junction migrated past the southern margin of the Sierra Nevada block between 16 and 18 Ma and the western margin of North America became a strike-slip boundary (Atwater & Stock, 1998; DeMets & Merkouriev, 2016; McQuarrie & Wernicke, 2005). The change in tectonic setting between the Pacific and North American plates altered the Sierra Nevada block's role as a boundary condition on the western Great Basin (Sonder & Jones, 1999). The Sierra Nevada went from being a passive

boundary of the extending Basin and Range to becoming a rigid strike-slip boundary. Since this change around 16 Ma, the portion of shear between the Pacific and North American plates that is transferred across the rigid Sierra Nevada block concentrates in the Walker Lane (Figure 2) due to the nonlinear rheology of the lithosphere.

The timing of this change coincides with the first documented evidence of strike-slip in the Walker Lane, at 13 Ma in the Las Vegas Valley shear zone and on the Stateline fault (Faulds & Henry, 2008; Guest et al., 2007), the northwestward progression of shear in the Walker Lane (Busby, 2013; Faulds & Henry, 2008; McQuarrie & Wernicke, 2005; Wernicke & Snow, 1998), and the onset of clockwise rotation (e.g., Cashman & Fontaine, 2000). Millions of years of extension since ~35–16 Ma and shear since ~13 Ma weakened the crust of the western Great Basin and encouraged both shear and extension to concentrate in the west today. Thus, tectonic evolution of the Pacific-North America plate boundary, the rate of relative strike-slip between the Pacific and North American plates, the nonlinear rheology of western US lithosphere, and the existence of the rigid Sierra Nevada block together account for the modern observations from both fault and GPS data of strain concentration in the Walker Lane.

5.4. Implications for Seismic Hazard

The faults of the Walker Lane comprise the surface expression of a zone of concentrated, continuous straining. Since the geologic record of shear in the Walker Lane is incomplete, known faults may not give the complete history, and hazard calculations based solely on known faults may underestimate hazard. For example, if measurements of strike-slip offset underestimate displacement from past earthquakes (e.g., Reitman et al., 2019), those earthquakes are likely to be larger than estimated from the paleoseismic record. Furthermore, documenting previously unidentified faults (e.g., Dong et al., 2014) increases the number of earthquake sources and regions that may be prone to moderate or strong earthquakes in the future from earthquakes on these smaller faults. Since there are few long strike-slip faults in the Walker Lane (Wesnousky et al., 2012), strike slip may occur mostly on shorter faults that are not capable of producing large (≥M7) earthquakes, and therefore slip in more frequent moderate earthquakes than in rarer larger ones (Anderson, 1979; Molnar, 1979). More frequent moderate earthquakes may pose greater hazard than fewer large earthquakes (Minson et al., 2020; Valentini et al., 2020). If missing strike slip is accommodated by moderate earthquakes that do not always rupture the surface (e.g., the 2020 Monte Cristo earthquake and dePolo, 1994), seismic hazard in the Walker Lane may be higher than estimates based solely on the paleoseismic record.

The Walker Lane strains more than its surroundings because the nonlinear rheology of the lithosphere concentrates strain close to the edge of the rigid Sierra Nevada boundary. The Walker Lane is therefore a zone of elevated hazard with an incomplete geologic record of shear. Probabilistic seismic hazard models based on fault slip rates determined by GPS and the paleoseismic record of known faults (Petersen et al., 2013, 2014) could consider the possibility of earthquakes occurring on smaller nearby faults or unmapped faults. Implementing a polygon or zone in hazard models, such as the 2008 version of the USGS National Seismic Hazard Map (Petersen et al., 2008) and Version 3 of the Uniform California Earthquake Rupture Forecast (Field et al., 2013), may better account for unidentified seismic sources and distributed deformation known to occur within the Walker Lane.

6. Conclusion

Strain and velocity calculated from 15-ka fault slip rates show similar patterns to horizontal GPS velocities across the Great Basin, with the fastest straining in the Walker Lane within ~150 km of the Sierra Nevada front. The similarity between the velocity fields inferred from geologic and geodetic data suggests that the pattern of deformation has been constant over the past 15 Kyr. The different rates of horizontal velocity across the Walker Lane suggest that evidence of shear is missing from the geologic record, and the mismatch cannot be due to crustal block rotations or transient strain rates. The missing shear is likely due to a combination of slip on unidentified strike-slip faults, undocumented strike-slip components on normal faults, distributed strain, and slip in moderate size earthquakes invisible to the paleoseismic record. The

distribution of straining is consistent with the onset of shear in the Walker Lane around 13 Ma, after the Mendocino triple junction migrated past the southern margin of the more rigid Sierra Nevada block and strain began concentrating in the western Great Basin. The Neogene tectonic history of western North America, fault slip rates since 15 ka, and modern GPS velocities provide a strong argument to view western US tectonics as continuous deformation of a nonlinear (n = 4–9) thin viscous sheet with the rigid Sierra Nevada block acting as a shear boundary of the western Great Basin and concentrating strain within the Walker Lane.

Data Availability Statement

Data generated in the analysis, input fault source parameters, and the script used to calculate strain and velocity are archived online at: https://doi.org/10.5281/zenodo.3895334. Other datasets used in the analysis and figures are publicly available from the following sources. The neotectonic database from Pérouse and Wernicke (2017) is available as a supplement to their study. The USGS National Seismic Hazard Model source faults database is available at https://doi.org/10.5066/P9WUTEBT. MAGNET GPS data were downloaded from https://geodesy.unr.edu/magnet/Table3web.html on 12/18/2019. UNAVCO GAGE GPS data were downloaded from https://www.unavco.org/data/gps-gnss/derived-products/derived-products.html on 12/18/2019. The shapefile outline of the Great Basin was downloaded from https://www.nbmg.unr.edu/Geothermal/Data.html on 1/23/2019. State boundaries and the DEM of the western U.S. were downloaded from the National Map (https://viewer.nationalmap.gov/basic/) in 2018.

Acknowledgments
We thank Anke Friedrich for a thorough review of the paper and Craig Jones for general guidance and acquainting of material that we had overlooked. This material is based on work supported by the National Science Foundation Graduate Research Fellowship Program under Grant DGE-1650115 to NGR.

References

Abdrakhmatov, K. E., Walker, R. T., Campbel, G. E., Carr, A. S., Elliott, A., Hillemann, C., et al. (2016). Multisegment rupture in the 11 July 1889 Chilik earthquake (Mw 8.0–8.3), Kazakh Tien Shan, interpreted from remote sensing, field survey, and paleoseismic trenching. *Journal of Geophysical Research: Solid Earth*, *121*, 1–16. https://doi.org/10.1002/2015JB012763

Aki, K., & Richards, P. G. (2002). *Quantitative seismology*. Sausalito, CA: University Science Books.

Anderson, J. G. (1979). Estimating the seismicity from geological structure for seismic-risk studies. *Bulletin of the Seismological Society of America*, *69*, 135–158.

Angster, S. J., Wesnousky, S. G., Figueiredo, P. M., Owen, L. A., & Hammer, S. J. (2019). Late Quaternary slip rates for faults of the central Walker Lane (Nevada, USA): Spatiotemporal strain release in a strike-slip fault system. *Geosphere*, *15*, 1–19. https://doi.org/10.1130/GES02088.1

Angster, S. J., Wesnousky, S., Huang, W. L., Kent, G., Nakata, T., & Goto, H. (2016). Application of UAV photography to refining the slip rate on the Pyramid Lake fault zone, Nevada. *Bulletin of the Seismological Society of America*, *106*, 785–798. https://doi.org/10.1785/0120150144

Atwater, T. (1970). Implications of plate tectonics in the Cenozoic tectonic evolution of western North America. *The Geological Society of America Bulletin*, *81*, 3513–3536. https://doi.org/10.1130/0016-7606(1970)81

Atwater, T., & Stock, J. (1998). Pacific-North America plate tectonics of the Neogene southwestern United States: An update. *International Geology Review*, *40*, 375–402. https://doi.org/10.1080/00206819809465216

Bahadori, A., & Holt, W. E. (2019). Geodynamic evolution of southwestern North America since the Late Eocene. *Nature Communications*, *10*, 1–18. https://doi.org/10.1038/s41467-019-12950-8

Bahadori, A., Holt, W. E., & Rasbury, E. T. (2018). Reconstruction modeling of crustal thickness and paleotopography of western North America since 36 Ma. *Geosphere*, *14*. https://doi.org/10.1130/GES01604.1

Baljinnyam, I., Bayasgalan, A., Borisov, B. A., Cisternas, A., Dem'yanovich, M. G., Ganbaatar, L., et al. (1993). Ruptures of major earthquakes and active deformation in Mongolia and its surroundings. *Memoirs – Geological Society of America*, *181*, 62. https://doi.org/10.1130/MEM181

Bennett, R. A., Wernicke, B. P., Niemi, N. A., Friedrich, A. M., & Davis, J. L. (2003). Contemporary strain rates in the northern Basin and Range province from GPS data. *Tectonics*, *22*. https://doi.org/10.1029/2001TC001355

Blewitt, G., Hammond, W. C., & Kreemer, C. (2018). Harnessing the GPS data explosion for interdisciplinary science. *Eos*, *99*. https://doi.org/10.1029/2018EO104623

Bormann, J. M., Hammond, W. C., Kreemer, C., & Blewitt, G. (2016). Accommodation of missing shear strain in the Central Walker Lane, western North America: Constraints from dense GPS measurements. *Earth and Planetary Science Letters*, *440*, 169–177. https://doi.org/10.1016/j.epsl.2016.01.015

Busby, C. J. (2013). Birth of a plate boundary at ca. 12 Ma in the Ancestral Cascades arc, Walker Lane belt of California and Nevada. *Geosphere*, *9*, 1147–1160. https://doi.org/10.1130/GES00928.1

Carlson, C. W., Pluhar, C. J., Glen, J. M. G., & Farner, M. J. (2013). Kinematics of the west-central walker lane: Spatially and temporally variable rotations evident in the late miocene stanislaus group. *Geosphere*, *9*, 1530–1551. https://doi.org/10.1130/GES00955.1

Cashman, P. H., & Fontaine, S. A., 2000, Strain partitioning in the northern Walker Lane, western Nevada and northeastern California. *Tectonophysics*, *326*, 111–130. https://doi.org/10.1016/S0040-1951(00)00149-9

Caskey, S. J., Wesnousky, S. G., Zhang, P., & Slemmons, D. B. (1996). Surface faulting of the 1954 Fairview Peak (Ms 7.2) and Dixie Valley (Ms 6.8) earthquakes, central Nevada. *Bulletin of the Seismological Society of America*, *86*, 761–787.

Choi, J.-H. H., Klinger, Y., Ferry, M., Ritz, J.-F. F., Kurtz, R., Rizza, M., et al. (2018). Geologic inheritance and earthquake rupture processes: The 1905 M≥8 Tsetserleg-Bulnay strike-slip earthquake sequence, Mongolia. *Journal of Geophysical Research: Solid Earth*, *123*, 1925–1953. https://doi.org/10.1002/2017JB013962

Colgan, J. P., Johnstone, S. A., & Shuster, D. L. (2020). Timing of Cenozoic extension in the southern Stillwater Range and Dixie Valley, Nevada. *Tectonics*, *29*, 1–18. https://doi.org/10.1029/2019TC005757

Crone, A. J., Machette, M. N., Bonilla, M. G., Lienkaemper, J. J., Pierce, K. L., Scott, W. E., et al. (1987). Surface faulting accompanying the Borah Peak earthquake and segmentation of the Lost River fault, central Idaho. *Bulletin of the Seismological Society of America*, *77*, 739–770.

DeMets, C., & Merkouriev, S. (2016). High-resolution reconstructions of Pacific-North America plate motion: 20 Ma to present. *Geophysical Journal International*, *207*, 741–773. https://doi.org/10.1093/gji/ggw305

dePolo, C. M. (1994). The maximum background earthquake for the Basin and Range province, western North America. *Bulletin of the Seismological Society of America*, *84*, 466–472.

dePolo, C. M., & Anderson, J. G. (2000). Estimating the slip rates of normal faults in the Great Basin, USA. *Basin Research*. *12*, 227–240. https://doi.org/10.1111/j.1365-2117.2000.00131.x

Dixon, T. H., Miller, M., Farina, F., Wang, H., & Johnson, D. (2000). Present-day motion of the Sierra Nevada block and some tectonic implications for the Basin and Range province, North American Cordillera. *Tectonics*, *19*, 1–24. https://doi.org/10.1029/1998TC001088

Dokka, R. K., & Travis, C. J. (1990). Late Cenozoic strike-slip faulting in the Mojave Desert, California. *Tectonics*, *9*, 311–340. https://doi.org/10.1029/TC009i002p00311

Dong, S., Ucarkus, G., Wesnousky, S. G., Maloney, J., Kent, G., Driscoll, N., & Baskin, R. (2014). Strike-slip faulting along the Wassuk Range of the northern Walker Lane, Nevada. *Geosphere*, *10*, 40–48. https://doi.org/10.1130/GES00912.1

Duross, C. B., Gold, R. D., Dawson, T. E., Scharer, K., Kendrick, K., Akciz, S., et al. (2020). Surface displacement distributions for the July 2019 Ridgecrest, California, earthquake ruptures. *Bulletin of the Seismological Society of America*. *110*, 1400–1418. https://doi.org/10.1785/0120200058

Ekström, G., & England, P. (1989). Seismic strain rates in regions of distributed continental deformation. *Journal of Geophysical Research*, *94*, 10231–10257. https://doi.org/10.1029/JB094iB08p10231

England, P., Houseman, G., & Sonder, L. (1985). Length scale for continental deformation in convergent, divergent, and strike-slip environments: Analytical and approximate solution for a thin viscous sheet model. *Journal of Geophysical Research*, *90*, 3551–3557. https://doi.org/10.1029/JB090iB05p03551

England, P., & Molnar, P. (1997). The field of crustal velocity in Asia calculated from Quaternary rates of slip on faults. *Geophysical Journal International*, *130*, 551–582.

England, P., & Molnar, P. (2005). Late Quaternary to decadal velocity fields in Asia. *Journal of Geophysical Research*, *110*, 1–27. https://doi.org/10.1029/2004JB003541

Evans, E. L., Loveless, J. P., & Meade, B. J. (2015). Total variation regularization of geodetically and geologically constrained block models for the Western United States. *Geophysical Journal International*, *202*, 713–727. https://doi.org/10.1093/gji/ggv164

Evans, E. L., Thatcher, W. R., Pollitz, F. F., & Murray, J. R. (2016). Persistent slip rate discrepancies in the eastern California (USA) shear zone. *Geology*, *44*, 691–694. https://doi.org/10.1130/G37967.1

Faulds, J. E., & Henry, C. D. (2008). Tectonic influences on the spatial and temporal evolution of the Walker Lane: An incipient transform fault along the evolving Pacific–North American plate boundary. In J. E. Spencer, & S. R. Titley (Eds.), Ores and orogenesis: Circum-Pacific tectonics, geologic evolution, and ore deposits, (Vol. 22, pp. 437–470). Arizona Geological Society Digest.

Field, E. H., Biasi, G. P., Bird, P., Dawson, T. E., Felzer, K. R., Jackson, D. D., et al. (2013). *The Uniform California Earthquake Rupture Forecast, version 3 (UCERF3) – The time-independent model*, (Open-File Report 2013-1165, pp. 97). U.S. Geological Survey. Retrieved from https://pubs.usgs.gov/of/2013/1165/

Florensov, N. A., & Solonenko, V. P. (Eds.), (1963). *The Gobi-Altai Earthquake (in Russian)*, (pp. 391). Moscow: Nauk USSR.

Frankel, K. L., Dolan, J. F., Owen, L. A., Ganev, P., & Finkel, R. C. (2011). Spatial and temporal constancy of seismic strain release along an evolving segment of the Pacific-North America plate boundary. *Earth and Planetary Science Letters*, *304*, 565–576. https://doi.org/10.1016/j.epsl.2011.02.034

Friedrich, A. M., Wernicke, B. P., Niemi, N. A., Bennett, R. A., & Davis, J. L. (2003). Comparison of geodetic and geologic data from the Wasatch region, Utah, and implications for the spectral character of Earth deformation at periods of 10 to 10 million years. *Journal of Geophysical Research*, *108*, 2199. https://doi.org/10.1029/2001JB000682

Gilbert, H. (2012). Crustal structure and signatures of recent tectonism as influenced by ancient terranes in the western United States. *Geosphere*, *8*, 141–157. https://doi.org/10.1130/GES00720.1

Gold, R. D., Briggs, R. W., Personius, S. F., Crone, A. J., Mahan, S. A., & Angster, S. J. (2014). Latest Quaternary paleoseismology and evidence of distributed dextral shear along the Mohawk Valley fault zone, northern Walker Lane, California Ryan. *Journal of Geophysical Research: Solid Earth*, *119*, 5014–5032. https://doi.org/10.1002/2014JB010987.Received

Gold, R. D., dePolo, C. M., Briggs, R. W., Crone, A. J., & Gosse, J. (2013a). Late quaternary slip-rate variations along the Warm Springs Valley fault system, northern Walker Lane, California-Nevada border. *Bulletin of the Seismological Society of America*, *103*, 542–558. https://doi.org/10.1785/0120120020

Gold, R. D., Reitman, N. G., Briggs, R. W., Barnhart, W. D., Hayes, G. P., & Wilson, E. (2015). On- and off-fault deformation associated with the September 2013 Mw 7.7 Balochistan earthquake: Implications for geologic slip rate measurements. *Tectonophysics*, *660*, 65–78. https://doi.org/10.1016/j.tecto.2015.08.019

Gold, R. D., Stephenson, W. J., Odum, J. K., Briggs, R. W., Crone, A. J., & Angster, S. J. (2013b). Concealed Quaternary strike-slip fault resolved with airborne lidar and seismic reflection: The Grizzly Valley fault system, northern Walker Lane, California. *Journal of Geophysical Research: Solid Earth*, *118*, 3753–3766. https://doi.org/10.1002/jgrb.50238

Grow, J. (2009). *Paleomagnetic data bearing on the evolution of the Walker Lane Belt transfer zone from mid-Miocene to present: An investigation of the inferred southern and eastern boundaries*, (pp. 67). https://digitalrepository.unm.edu/eps_etds/32

Guest, B., Niemi, N., & Wernicke, B. (2007). Stateline fault system: A new component of the Miocene-Quaternary eastern California shear zone. *Bulletin of the Geological Society of America*, *119*, 1337–1346. https://doi.org/10.1130/0016-7606(2007)119[1337:SFSANC]2.0.CO

Haines, A. J. (1982). Calculating velocity fields across plate boundaries from observed shear rates. *Geophysical Journal International*, *68*, p. 203–209.

Haines, A. J., & Holt, W. E. (1993). A Procedure for obtaining the complete horizontal motions within zones of distributed deformation from the inversion of strain rate data. *Journal of Geophysical Research*, *98*, 12057–12082. https://doi.org/10.1029/93JB00892

Hammond, W. C., Blewitt, G., & Kreemer, C. (2011). Block modeling of crustal deformation of the northern Walker Lane and Basin and Range from GPS velocities. *Journal of Geophysical Research*, *116*, 1–28. https://doi.org/10.1029/2010JB007817

Hammond, W. C., Blewitt, G., & Kreemer, C. (2014). Steady contemporary deformation of the central Basin and Range Province, western United States. *Journal of Geophysical Research: Solid Earth*, *119*, 1–19. https://doi.org/10.1002/2014JB011145.Received

Hammond, W. C., & Thatcher, W. (2007). Crustal deformation across the Sierra Nevada, northern Walker Lane, Basin and Range transition, western United States measured with GPS, 2000–2004. *Journal of Geophysical Research*, *112*, 2000–2004. https://doi.org/10.1029/2006JB004625

Hanks, T. C., & Wallace, R. E. (1985). Morphological analysis of the Lake Lahontan shoreline and beachfront fault scarps, Pershing county, Nevada. *Bulletin of the Seismological Society of America*, *75*, 835–846.

Herring, T. A., Melbourne, T. I., Murray, M. H., Floyd, M. A., Szeliga, W. M., King, R. W., et al. (2016). Plate boundary observatory and related networks: GPS data analysis methods and geodetic products. *Reviews of Geophysics*, *54*, 1–50. https://doi.org/10.1002/2016RG000529

Holt, W. E., Ni, J. F., Wallace, T. C., & Haines, A. J. (1991). The active tectonics of the eastern Himalayan syntaxis and surrounding regions. *Journal of Geophysical Research*, *96*, 14595–14632. https://doi.org/10.1029/91JB01021

Jackson, J., & McKenzie, D. (1988). The relationship between plate motions and seismic moment tensors, and the rates of active deformation in the Mediterranean and Middle East. *Geophysical Journal International*, *93*, 45–73.

Koehler, R. D., Dee, S., Elliott, A., Hatem, A., Pickering, A., Pierce, I., et al. (2021). Field response and surface-rupture characteristics of the 2020 M 6.5 Monte Cristo Range earthquake, Central Walker Lane, Nevada. *Seismological Research Letters*, 1–17. https://doi.org/10.1785/0220200371

Koehler, R. D., & Wesnousky, S. G. (2011). Late Pleistocene regional extension rate derived from earthquake geology of late Quaternary faults across the Great Basin, Nevada, between 38.5°N and 40°N latitude. *The Geological Society of America Bulletin*, *123*, 631–650. https://doi.org/10.1130/B30111.1

Kostrov, V. V. (1974). Seismic moment and energy of earthquakes and seismic flow of rock. *Earth Physics*, *1*, 23–40.

Kreemer, C. (2009). Geodetic constraints on contemporary deformation in the northern Walker Lane: 2. Velocity and strain rate tensor analysis. *Special Paper of the Geological Society of America*, *447*, 17–31. https://doi.org/10.1130/2009.2447(02)

Kreemer, C., Blewitt, G., & Klein, E. C. (2014). A geodetic plate motion and global strain rate model. *Geochemistry, Geophysics, Geosystems*, *15*, 3849–3889. https://doi.org/10.1002/2014GC005407

Kurushin, R. A., Bayasgalan, A., Ölziybat, M., Enhtuvshin, B., Molnar, P., Bayarsayhan, C., et al. (1997). The surface rupture of the 1957 Gobi-Altay, Mongolia, earthquake: Boulder, Colorado. *Geological Society of America Special Paper*. *320*, 1–144. https://doi.org/10.1130/0-8137-2320-5.1

Lifton, Z. M., Frankel, K. L., & Newman, A. V. (2015). Latest Pleistocene and Holocene slip rates on the Lone Mountain fault: Evidence for accelerating slip in the Silver Peak-Lone Mountain extensional complex. *Tectonics*, *34*, 449–463. https://doi.org/10.1002/2013TC003512

Lifton, Z. M., Lee, J., Frankel, K., Newman, A. V., & Schroeder, J. M. (2020). Quaternary slip rates on the White Mountains fault zone, eastern California: Implications for comparing geologic to geodetic slip rates across the Walker Lane. *Bulletin of the Geological Society of America*, *133*, 307–324. https://doi.org/10.1130/B35332.1

Lifton, Z. M., Newman, A. V., Frankel, K. L., Johnson, C. W., & Dixon, T. H. (2013). Insights into distributed plate rates across the Walker Lane from GPS geodesy. *Geophysical Research Letters*, *40*, 4620–4624. https://doi.org/10.1002/grl.50804

Locke, A., Billingsley, P., & Mayo, E. B. (1940). Sierra Nevada tectonic pattern. *Bulletin of the Geological Society of America*, *51*, 513–540.

Long, S. P. (2019). Geometry and magnitude of extension in the Basin and Range Province (39°N), Utah, Nevada, and California, USA: Constraints from a province-scale cross section. *The Geological Society of America Bulletin*, *131*, 99–119.

McKenzie, D., & Jackson, J. (1983). The relationship between strain rates, crustal thickening, paleomagnetism, finite strain and fault movements within a deforming zone. *Earth and Planetary Science Letters*, *65*, 182–202.

McQuarrie, N., & Wernicke, B. P. (2005). An animated Tectonic Reconstruction of Southwestern North America since 36 Ma. *Geosphere*, *1*, 147–172. https://doi.org/10.1130/GES00016.1

Meade, B. J., & Hager, B. H. (2005). Block models of crustal motion in southern California constrained by GPS measurements. *Journal of Geophysical Research B*, *110*, 1–19. https://doi.org/10.1029/2004JB003209

Milliner, C. W. D., Dolan, J. F., Hollingsworth, J., Leprince, S., & Ayoub, F. (2016). Comparison of coseismic near-field and off-fault surface deformation patterns of the 1992 Mw 7.3 Landers and 1999 Mw 7.1 Hector Mine earthquakes: Implications for controls on the distribution of surface strain. *Geophysical Research Letters*, *43*, 10115–10124. https://doi.org/10.1002/2016GL069841

Minson, S. E., Baltay, A. S., Cochran, E. S., McBride, S. K., & Milner, K. R. (2020). Shaking is almost always a surprise: The earthquakes that produce significant ground motion. *Seismological Research Letters*, *92*, 460–468. https://doi.org/10.1785/0220200165

Molnar, P. (1979). Earthquake recurrence intervals and plate tectonics. *Bulletin of the Seismological Society of America*, *69*, 115–133.

Molnar, P. (1983). Average regional strain due to slip on numerous faults of different orientations. *Journal of Geophysical Research*, *88*, 6430–6432.

Molnar, P., & Deng, Q. (1984). Faulting associated with large earthquakes and the average rate of deformation in central and eastern Asia. *Journal of Geophysical Research*, *89*, 6203–6227. https://doi.org/10.1029/JB088iB08p06430

Oldow, J. S., Geissman, J. W., & Stockli, D. F. (2008). Evolution and strain reorganization within Late Neogene structural stepovers linking the central Walker Lane and northern eastern California shear zone, western Great Basin. *International Geology Review*, *50*, 270–290. https://doi.org/10.2747/0020-6814.50.3.270

Parsons, T., & Thatcher, W. (2011). Diffuse Pacific-North American plate boundary: 1000 km of dextral shear inferred from modeling geodetic data. *Geology*, *39*, 943–946. https://doi.org/10.1130/G32176.1

Pérouse, E., & Wernicke, B. P. (2017). Spatiotemporal evolution of fault slip rates in deforming continents: The case of the Great Basin region, northern Basin and Range province. *Geosphere*, *13*, 112–135. https://doi.org/10.1130/GES01295.1

Personius, S. F., Briggs, R. W., Maharrey, J. Z., Angster, S. J., Mahan, S. A., & Forest, P. (2017). A Paleoseismic Transect across the Northwestern Basin and Range Province, Northwestern Nevada and Northeastern California, USA. *Geosphere*, *13*, 782–810. https://doi.org/10.1130/GES01380.1

Petersen, M. D., Frankel, A. D., Harmsen, S. C., Mueller, C. S., Haller, K. M., Wheeler, R. L., et al. (2008). *Documentation for the 2008 update of the United States National Seismic Hazard Maps*, (Open-File Report 2008-1128, pp. 61). U.S. Geological Survey. https://doi.org/10.3133/ofr20081128

Petersen, M. D., Moschetti, M. P., Powers, P. M., Mueller, C. S., Haller, K. M., Frankel, A. D., et al. (2014). *Documentation for the 2014 update of the United States National Seismic Hazard Maps*, (Open-File Report 2014-1091, pp. 243). U.S. Geological Survey. https://doi.org/10.3133/ofr20141091

Petersen, M. D., Shumway, A. M., Powers, P. M., Mueller, C. S., Moschetti, M. P., Frankel, A. D., et al. (2020). The 2018 update of the US National Seismic Hazard Model: Overview of model and implications. *Earthquake Spectra*, *36*, 5–41. https://doi.org/10.1177/8755293019878199

Petersen, M. D., Zeng, Y., Haller, K. M., McCaffrey, R., Hammond, W. C., Bird, P., et al. (2013). *Geodesy- and geology-based slip-rate models for the western United States (excluding California) National Seismic Hazard Maps*, (Open-File Report 2013-1293, pp. 80). U.S. Geological Survey. https://doi.org/10.3133/ofr20131293

Petronis, M. S., Geissman, J. W., Oldow, J. S., & Mcintosh, W. C. (2009). Late Miocene to Pliocene vertical-axis rotation attending development of the Silver Peak-Lone Mountain displacement transfer zone, west-central Nevada. *Geological Society of America Special Paper*, *447*, 215–253. https://doi.org/10.1130/2009.2447(12)

Pluhar, C. J., Coe, R. S., Lewis, J. C., Monastero, F. C., & Glen, J. M. G. (2006). Fault block kinematics at a releasing stepover of the Eastern California shear zone: Partitioning of rotation style in and around the Coso geothermal area and nascent metamorphic core complex. *Earth and Planetary Science Letters*, *250*, 134–163. https://doi.org/10.1016/j.epsl.2006.07.034

Powers, P. (2020). *nshm-fault-sections, Version 1.0* (Source code). https://doi.org/10.5066/P9WUTEBT

Reheis, M. C., & Sawyer, T. L. (1997). Late Cenozoic history and slip rates of the Fish Lake Valley, Emigrant Peak, and deep Springs fault zones, Nevada and California. *Bulletin of the Geological Society of America*, *109*, 280–299. https://doi.org/10.1130/0016-7606(1997)109

Reitman, N. G., Mueller, K. J., Tucker, G. E., Gold, R. D., Briggs, R. W., & Barnhart, K. R. (2019). Offset channels may not accurately record strike-slip fault displacement: Evidence from landscape evolution models. *Journal of Geophysical Research: Solid Earth*, *124*, 13427–13451. https://doi.org/10.1029/2019JB018596

Rood, D. H., Burbank, D. W., Herman, S. W., & Bogue, S. (2011). Rates and timing of vertical-axis block rotations across the central Sierra Nevada-Walker Lane transition in the Bodie Hills, California/Nevada. *Tectonics*, *30*, 1–23. https://doi.org/10.1029/2010TC002754

Sonder, L. J., & England, P. (1986). Vertical averages of rheology of the continental lithosphere: Relation to thin sheet parameters. *Earth and Planetary Science Letters*, *77*, 81–90.

Sonder, L. J., & Jones, C. H. (1999). Western United States extension: How the west was widened. *Annual Review of Earth and Planetary Sciences*, *27*, 417–462.

Stein, S., & Friedrich, A. M. (2014). How much can we clear the crystal ball? *Astronomy and Geophysics*, *55*, 11–17. https://doi.org/10.1093/astrogeo/atu076

Stewart, J. H. (1980). *Geology of Nevada: A Discussion to accompany the Geologic Map of Nevada*, (Vol. 4). Nevada Bureau of Mines and Geology Special Publication.

Stewart, J. H. (1988). Tectonics of the Walker Lane Belt, western Great Basin: Mesozoic and Cenozoic deformation in a zone of shear. In W. Ernst (Ed.), *Metamorphism and crustal evolution of the western United States*.

Surpless, B. E., & Kroeger, G. (2014). The unusual temporal and spatial slip history of the Wassuk Range normal fault, western Nevada (USA): Implications for seismic hazard and Walker lane deformation. *Bulletin of the Geological Society of America*, *127*, 737–758. https://doi.org/10.1130/B31159.1

Surpless, B. E., Stockli, D. F., Dumitru, T. A., & Miller, E. L. (2002). Two-phase westward encroachment of Basin and Range extension into the northern Sierra Nevada. *Tectonics*, *21*. https://doi.org/10.1029/2000TC001257

Valentini, A., Duross, C. B., Field, E. H., Gold, R. D., Briggs, R. W., Visini, F., et al. (2020). Relaxing segmentation on the Wasatch fault zone: Impact on seismic hazard. *Bulletin of the Seismological Society of America*, *110*, 83–109. https://doi.org/10.1785/0120190088

Wernicke, B., & Snow, J. K. (1998). Cenozoic tectonism in the central Basin and Range: Motion of the Sierran-Great Valley block. *International Geology Review*, *40*, 403–410. https://doi.org/10.1080/00206819809465217

Wesnousky, S. G. (2005). Active faulting in the Walker Lane. *Tectonics*, *24*, 1–35. https://doi.org/10.1029/2004TC001645

Wesnousky, S. G., Barron, A. D., Briggs, R. W., Caskey, S. J., Kumar, S., & Owen, L. (2005). Paleoseismic transect across the northern Great Basin. *Journal of Geophysical Research*, *110*, 1–26. https://doi.org/10.1029/2004JB003283

Wesnousky, S. G., Bormann, J. M., Kreemer, C., Hammond, W. C., & Brune, J. N. (2012). Neotectonics, geodesy, and seismic hazard in the Northern Walker Lane of Western North America: Thirty kilometers of crustal shear and no strike-slip? *Earth and Planetary Science Letters*, *329–330*, 133–140. https://doi.org/10.1016/j.epsl.2012.02.018

Whitehouse, P. L., England, P. C., & Houseman, G. A. (2005). A physical model for the motion of the Sierra Block relative to North America. *Earth and Planetary Science Letters*, *237*, 590–600. https://doi.org/10.1016/j.epsl.2005.03.028

Zheng, A., Chen, X., & Xu, W. (2020). Present-day deformation mechanism of the northeastern Mina deflection revealed by the 2020 Mw 6.5 Monte Cristo Range earthquake. *Geophysical Research Letters*, *47*, 1–10. https://doi.org/10.1029/2020GL090142